

ORIGINAL ARTICLE

Full picture discovery for mixed-fluorine anion effects on high-voltage spinel lithium nickel manganese oxide cathodes

Dae-wook Kim^{1,4}, Hiromasa Shiiba^{1,4}, Nobuyuki Zetsu^{1,2}, Tetsuya Yamada², Takeshi Kimijima², Gabriel Sánchez-Santolino³, Ryo Ishikawa³, Yuichi Ikuhara³ and Katsuya Teshima^{1,2}

Small amounts of fluorine substituting for oxygen deficiencies could reduce Mn dissolution, enhancing the cyclability in spinel-type lithium nickel manganese oxides (LiNi_{0.5}Mn_{1.5}O₄). Fluorine anion incorporation simultaneously enhances the C-rate capability and specific capacity fading. We used experimental and theoretical approaches to obtain a full picture of the mixed-anion effects for LiNi_{0.5}Mn_{1.5}O_{4-x}F_x cathode materials. The fluorine anion reduced the activation barrier for lithium-ion hopping along the most energetically preferable 8a-16c-8a route, enhancing the C-rate capability. Simultaneously, the coordination bond of the linear F⁻-Mn³⁺-F⁻ (Mn@2F diagonal) arrangement increased the oxidation potential to 5.1 V (vs Li⁺/Li). This hampered full extraction of Li⁺ from the spinel lattice, which was triggered by the oxidation of Mn³⁺ below the cutoff voltage (3.5–4.8 V (vs Li⁺/Li)), leading to a capacity loss.

NPG Asia Materials (2017) 9, e398; doi:10.1038/am.2017.90; published online 7 July 2017

INTRODUCTION

Lithium (Li)-ion secondary batteries have improved our lifestyles over the past two decades.¹ However, the technical requirements for Li-ion secondary batteries are entering a phase of major change with respect to the energy density, which will require higher-energy-density cathode materials.² The cathode's energy density depends on the specific capacity, tap density, loading amount and average operating voltage of the active materials. High-voltage materials could reduce the number of serially connected cells and enhance the energy density.

Spinel-type LiNi_{0.5}Mn_{1.5}O₄ (LNMO) is a 5-V level high-voltage active material because of the high redox potential of Ni²⁺/Ni⁴⁺ (vs Li⁺/Li).^{3–6} LNMO can be crystallographically classified into two spinel structures: ordered *P4₃32* space group and disordered *Fd-3m* space group (cubic symmetry). Formation of an oxygen vacancy at the 24e site is critical for determining the symmetry and accompanying the reduction of Mn⁴⁺ to Mn³⁺ because of the charge balance. Recently, we performed density function theory (DFT) calculations to evaluate the formation energy using oxygen vacancy and metal-excess models for ordered and disordered LiNi_{0.5}Mn_{1.5}O_{4-δ} (LNMO_{4-δ}).⁷ Oxygen vacancy formation reactions were unlikely, although interstitial cation occupation occurred at the octahedral vacancies in both *P4₃32* and *Fd-3m* LNMO_{4-δ} spinel compounds.

The formation of Mn³⁺ in the LNMO lattice typically decreases the operating voltage, making the energy density lesser than that of stoichiometric LNMO.^{8–12} An excess of Mn³⁺ could produce

structural distortions and disproportionations, degrading the cycle capability during high-voltage operations.^{13–15} Alternatively, the ordered *P4₃32* phase has a limited power density. Low electron conductivity (two orders of magnitude lower than that of the *Fd-3m* LNMO) caused capacity fading in the high C-rate charge–discharge reaction.^{12,16,17}

We showed that tuning the Mn³⁺ concentration is important for suitable electrochemical characteristics. Substitution of the transition metal cation with Ni²⁺ and/or Mn⁴⁺ is a plausible way to tune the valence state of the manganese ion, which distributes defects in the spinel structure. Partial substitution of a cation (Cr, Fe, Mg, Zn or Ru) into the Ni and Mn sites provides a better performance than that of the pure structure.^{18–26}

Mixed-anion compounds (e.g., oxyfluoride) could enhance the electrochemical performance. A small amount of fluorine substitution for oxygen could reduce Mn dissolution (from hydrogen fluoride attack) and enhance the cyclability.^{27,28} The incorporation of fluorine anions (F⁻) simultaneously enhanced the C-rate capability and capacity fading.^{29,30} However, the origin of the enhanced electrochemical performance is not fully understood in relation to the electrical and structural properties,^{31–34} which are affected by the electronic and ionic conductivities. Because of the higher electronegativity, the F⁻ could interact with the Li⁺, causing an increased activation barrier for Li⁺ hopping along the 8a-16c-8a path in the spinel framework.

¹Department of Materials Chemistry, Faculty of Engineering, Shinshu University, Nagano, Japan; ²Center for Energy and Environmental Science, Shinshu University, Nagano, Japan and ³Institute of Engineering Innovation, The University of Tokyo, Tokyo, Japan

⁴These authors contributed equally to this work.

Correspondence: Professor N Zetsu or Professor K Teshima, Center for Energy and Environmental Science, Shinshu University, 4-17-1 Wakasato, 380-8553, Nagano, Japan. E-mail: zetsu@shinshu-u.ac.jp or teshima@shinshu-u.ac.jp

Received 19 December 2016; revised 23 February 2017; accepted 24 March 2017

Here, we address this contradictory issue for $\text{LiNi}_{0.5}\text{Mn}_{1.5}\text{O}_{4-x}\text{F}_x$ (LNMOF) cathode materials using experimental and theoretical approaches. Many fundamental studies have been carried out on cation-substitution effects, but there are only a few reports on mixed-anion effects. Therefore, determining the full picture for mixed-anion effects of high-voltage spinel systems provides new methods for material design that overcome the current performance limitations.

MATERIALS AND METHODS

Flux growth and characterization of LNMOF crystals

$\text{LNMO}_{4-\delta}$ crystals were grown by LiCl-KCl flux growth.³⁵ We performed a two-step flux growth for the LNMOF crystals with different amounts of fluorine substitution, including the flux growth of $\text{LNMO}_{4-\delta}$ crystals from the LiCl-KCl flux and subsequent fluorine anion incorporation in a molten KCl flux. For the incorporation of the fluorine anion, the $\text{LNMO}_{4-\delta}$ crystal was reacted with LiF in a KCl flux (800 °C, 20 h) at different LiF concentrations. The powders were washed with warm water to remove the remaining KCl flux and annealed under an O_2 atmosphere (700 °C, 10 h). The phases and structures of the crystals were identified using X-ray diffraction (XRD) analysis with a Cu-K α radiation source. The X-ray diffractometer (Miniflex II; Rigaku, Tokyo, Japan) was operated at 30 kV and 20 mA, with $2\theta=10\text{--}80^\circ$ (scan step=0.02). Field emission scanning electron microscopy (JSM-7600F at 15 kV; JEOL, Tokyo, Japan) observations were conducted to examine the microstructural characteristics in the crystals. The valence state of the Mn ion and atomic percent of incorporated fluorine atoms were studied by X-ray photoelectron spectroscopy (XPS) with a monochromic Al-K α source (JPS-9010MX at 15 kV, 15 mA; JEOL). All binding energies in the spectra were referenced to the C1s hydrocarbon peak at 284.5 eV. The etching thickness was controlled at 20 nm per Ar sputtering, which was calculated in relation to the silicon wafer. The orders of the Ni and Mn configurations were characterized by Raman spectroscopy with 532 nm excitation (LabRAM, Horiba, Japan). The electrochemical characteristics were evaluated using a coin-type cell (R2032-type). The cathode was prepared by a conventional pasting process and contained LNMOF crystals, acetylene black and polyvinylidene fluoride (90:5:5 wt%). The mixture was diluted with *N*-methyl-2-pyrrolidone to give a viscosity of ~ 5.1 Pa·s. The prepared paste was homogeneously coated onto a 20- μm -thick Al foil using a slit coater. The electrode density was adjusted to 3.0 g cm^{-3} using a press machine. All electrodes were dried at 120 °C in a vacuum oven before cell assembly. Li metal foil and a porous polypropylene film (#2500; Celgard, Charlotte, NC, USA) were used as the counter electrode and separator, respectively. A solution of 1 M LiPF_6 in a mixture of ethylene carbonate and dimethyl carbonate (1:1 vol.%) was used as the electrolyte. The coin-type cells were assembled in an Ar-filled glovebox (MDB-2BL; Miwa Mfg, Osaka, Japan) with a controlled atmosphere containing <1 p.p.m. H_2O and O_2 . The galvanostatic charge-discharge tests and electrochemical impedance spectroscopy (EIS) were performed using a potentiogalvanostat (HJ1020Msd8 (Hokuto Denko, Tokyo, Japan); VSP-300 (Bio-Logic, Seyssinet-Pariset, France)). The cutoff voltage range for the battery tests was controlled between 3.5 and 4.8 V vs Li/Li^+ . The frequency range for the EIS measurements was 1 MHz–0.001 Hz. All EIS measurements were performed at 23 °C in a constant-temperature chamber (SU-221; Espec, Hudsonville, MI, USA).

X-ray absorption fine-structure spectroscopy

Ex situ Mn K edge X-ray absorption fine-structure spectroscopy (XAFS) spectra were measured to evaluate the changes in the electrochemical states of the LNMOF crystal-based cathodes with different states of charge (SOCs) using the BL15A1 beamline of the Photon Factory (High Energy Accelerator Research Organization (KEK) in Tsukuba, Japan). The XAFS spectra were recorded from 6300 to 6900 eV in transmission mode. Each sample was measured for ~ 90 min. The spectral energy was calibrated using that of Mn_2O_3 . LNMOF electrodes were removed from a disassembled coin cell after three cycles and used as samples for the XAFS measurements. The SOCs were controlled at 0 and 75%, respectively, before disassembly. The capacities of these SOCs were carefully estimated from their first-cycle discharge capacities. We disassembled

the cells and washed them with dimethyl carbonate in an Ar-filled glove box. The samples were kept in a dried Ar atmosphere until the XAFS measurements.

DFT simulation

The DFT calculations were performed using the generalized gradient approximation (GGA-PBESol)+U and projector-augmented wave methods as implemented in the Vienna *ab initio* simulation package.^{36–39} The *U*-values for the *d*-orbitals of Ni and Mn were set to 6.0 and 3.9 eV, respectively.^{40–42} The magnetic ground state of LNMO exhibits ferrimagnetic ordering ($\text{Ni}\downarrow\text{Mn}\uparrow$), as reported in previous experimental and computational studies.^{31,43–45} Thus, the ferrimagnetic spin configurations were used for all the calculations in this study. An energy cutoff of 500 eV and a $3\times 3\times 3$ *k*-point mesh were used for the superstructure of 56 atoms in a cubic spinel lattice of $8(\text{LiNi}_{0.5}\text{Mn}_{1.5}\text{O}_4)$ with $P4_332$ symmetry as a starting structure. To realize the atomic arrangement of $8(\text{LiNi}_{0.5}\text{Mn}_{1.5}\text{O}_{4-x}\text{F}_x)$ ($0.125\leq x\leq 0.375$), we added 1–3 fluorine anions into the possible 24e and 8c O oxygen sites in the unit cell of $\text{LiNi}_{0.5}\text{Mn}_{1.5}\text{O}_{4-x}\text{F}_x$ ($0.125\leq x\leq 0.375$). The nudged elastic band method was used to investigate the minimum energy pathways of Li hopping from one lattice position to adjacent sites.^{46,47} Relaxation of the crystal structure was allowed for all calculations, and the final energies of the optimized geometries were recalculated to correct for changes of the plane-wave basis during relaxation.

Surface energy of the bulk model and surface model

We manually arranged the atoms on the LNMOF surface while retaining their crystallographic symmetry and chemical stoichiometry for calculating E_{slab} (the energy of a slab with a surface facet). The crystallographic symmetry of the top and bottom slab surfaces is essential for achieving a rational computational prediction. Therefore, the same analogy for calculating E_{slab} cannot be applied to the structures for $x=0.125$ and 0.375 because of their asymmetric O/F arrangement. In this work, we evaluated the surface energies for only $\text{LNMO}_{3.75}\text{F}_{0.25}$ ($x=0.25$).

The surface energies, γ , are defined as

$$\gamma = \frac{1}{2A} \left(E_{\text{slab}} - NE_{\text{bulk}} - \sum_{i=O,F} \Gamma_i \mu(i) \right), \quad (1)$$

where *A* is the surface area of slab, E_{bulk} is the energy per atom of the bulk model and *N* is the number of atoms in the slab model. The third term indicates the chemical potentials of excess or deficient oxygen and fluorine atoms for non-stoichiometric slab models. In this work, the chemical potentials of oxygen and fluorine were fixed as oxygen gas and fluorine gas, respectively, based on DFT calculations. The slab cells were constructed from the relaxed bulk structure, and the lattice parameters were fixed for the slab cells. For the calculations of the surface facets, slab thicknesses >20 Å were chosen for all facets with vacuum thicknesses of 20 Å.

Scanning transmission electron microscopy

Direct observation of an original atomic surface structure requires clean and electron transparent thin scanning transmission electron microscopy (STEM) specimens. We simply put the LNMOF powders in ethanol and dispersed them onto a perforated amorphous carbon grid, rather than using the conventional Ar-ion thinning method to avoid significant surface damages. The atomic-resolution annular bright-field (ABF) and annular dark-field (ADF) STEM images were acquired using an aberration-corrected JEM ARM300CF instrument (JEOL) installed at the University of Tokyo, equipped with a cold-field emission gun and electron energy-loss spectroscopy (EELS, Quantum; Gatan, Pleasanton, CA, USA). To suppress the beam damage to Li-containing materials, we operated our microscope at 80 kV at a relatively low-dose condition (~ 13 pA), and no significant structure changes were observed during image acquisition. The used convergence semiangle was 27 mrad and the collection angles were 13–27 and 70–200 mrad for ABF- and ADF-STEM imaging, respectively.

RESULTS AND DISCUSSION

Figures 1a–c shows the most stable O/F arrangements for (a) $x=0.125$, (b) $x=0.25$ and (c) $x=0.375$ in LNMOF. We

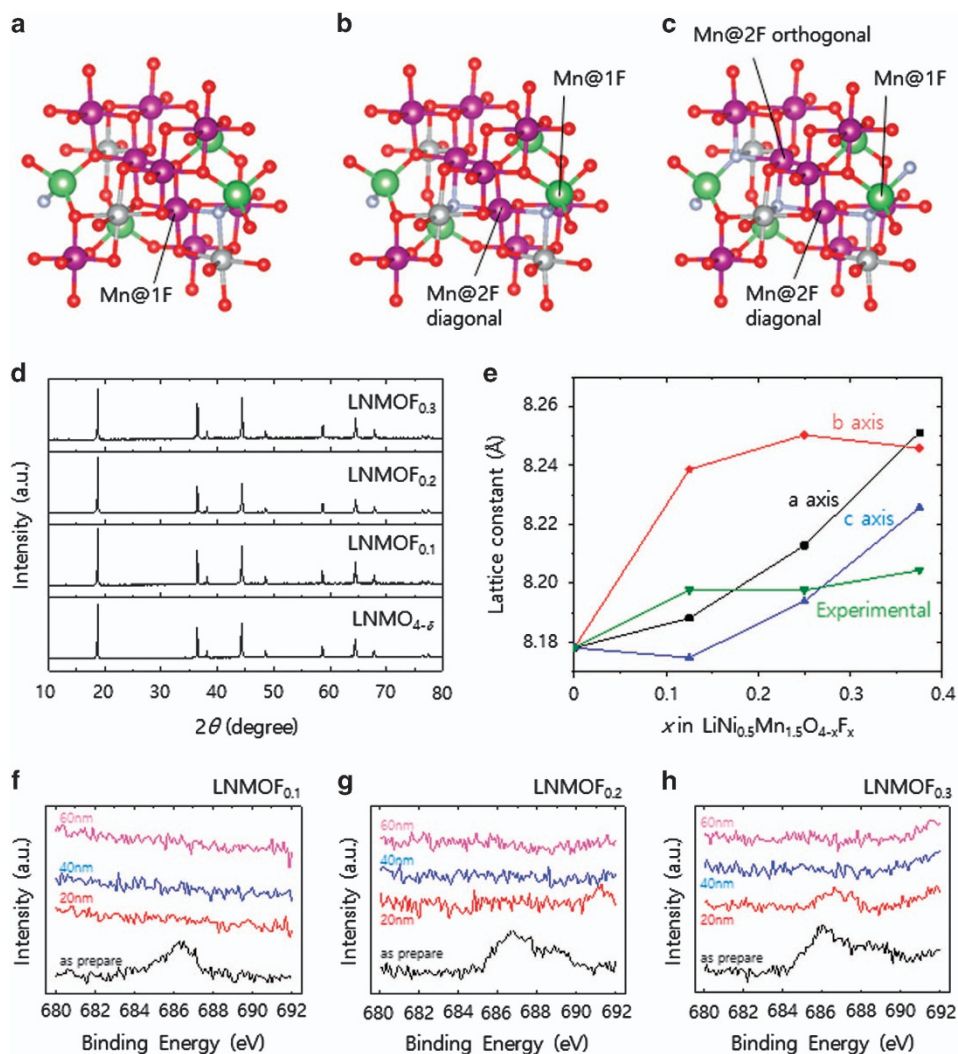


Figure 1 Experimental and computational studies on the fluorine anion distribution inside the spinel framework and the crystals of $\text{LiNi}_{0.5}\text{Mn}_{1.5}\text{O}_{4-x}\text{F}_x$ (LNMOF). All possible O/F arrangements were considered to determine the most stable 2, 13 and 9 different O/F arrangements, which were calculated for $x=0.125, 0.25$ and 0.375 , respectively: (a) $x=0.125$, (b) $x=0.25$ and (c) $x=0.375$ in $\text{LiNi}_{0.5}\text{Mn}_{1.5}\text{O}_{4-x}\text{F}_x$. (d) X-ray diffraction (XRD) patterns of LNMOF crystals with various amounts of fluorine anion incorporation. XRD patterns taken from all of the prepared samples are in good agreement with the reference data of ICDD PDF 70-8650 ($\text{LiNi}_{0.5}\text{Mn}_{1.5}\text{O}_4$) with a small shift from fluorine addition. (e) The lattice parameters of LNMOF determined from the XRD patterns and density function theory (DFT) calculations. Series of F1s X-ray photoelectron core-level spectra: (f) LNMOF_{0.1}, (g) LNMOF_{0.2} and (h) LNMOF_{0.3} with varying Ar sputtering etching thicknesses (black: as prepared; red: 20 nm; blue: 40 nm; and pink: 60 nm).

considered all possible O/F arrangements to determine the most stable arrangements; 2, 13 and 9 different O/F arrangements were calculated for $x=0.125, 0.25$ and 0.375 , respectively. The energy differences between the most stable and second most stable arrangements for $x=0.125, 0.25$ and 0.375 were 0.48, 0.29 and 0.07 eV, respectively. F^- preferentially occupied the 24e O sites instead of the 8c sites, independent of the amount of F^- substitution. The same tendency was noted for oxygen vacancy formation in the non-stoichiometric LNMO_{4-δ} system (e.g., the formation energy for 24e O site occupation in $\text{LiNi}_{0.5}\text{Mn}_{1.5}\text{O}_{3.875}\text{F}_{0.125}$ (LNMOF_{0.1}) was ~ 0.48 eV lower than that for 8c O site occupation). F^- coordinated with two Mn^{3+} ions and one Ni^{2+} ion. Furthermore, Mn^{4+} in the LNMO_{4-δ} lattice was reduced to Mn^{3+} as the same number of F^- ions was introduced into the structure. The incorporated F^- reduced the neighboring Mn^{4+} to Mn^{3+} . A linear F^- - Mn^{3+} - F^- cluster formed in $\text{LiNi}_{0.5}\text{Mn}_{1.5}\text{O}_{3.75}\text{F}_{0.25}$ (LNMOF_{0.2}) along the *b*-axis in octahedral MnO_6 (24e sites occupied by F^- (Mn@2F diagonal)). Further, incorporated F^- occupied other

nearest-neighboring 24e site. Two different configurations were formed in the $\text{LiNi}_{0.5}\text{Mn}_{1.5}\text{O}_{3.625}\text{F}_{0.375}$ (LNMOF_{0.3}) lattice (linear and bent for F^- - Mn^{3+} - F^- (Mn@2F neighbor) clusters in octahedral MnO_6). The bond length of Mn^{3+} - F^- in the Mn@2F diagonal arrangement was longer than that of the Mn@2F neighboring arrangement, indicating that Jahn-Teller distortion possibly elongated the direction of the Mn@2F diagonal arrangement (parallel to the *b*-axis).

The powder XRD patterns for all flux-growth samples were in good agreement with the reference data (ICDD PDF 70-8650; Figure 1d). All F^- -substituted LNMOF crystals were of single phase. Chemical composition analysis based on inductively coupled plasma optical emission spectrometry revealed that all the LNMOF crystals had almost stoichiometric compositions (Supplementary Table S1). The difference in the F contents for data obtained from the experiments and that used in the calculations are negligible from a crystallographic point of view. We used a superstructure composed of 56 atoms ($\text{F}_{0.125}$

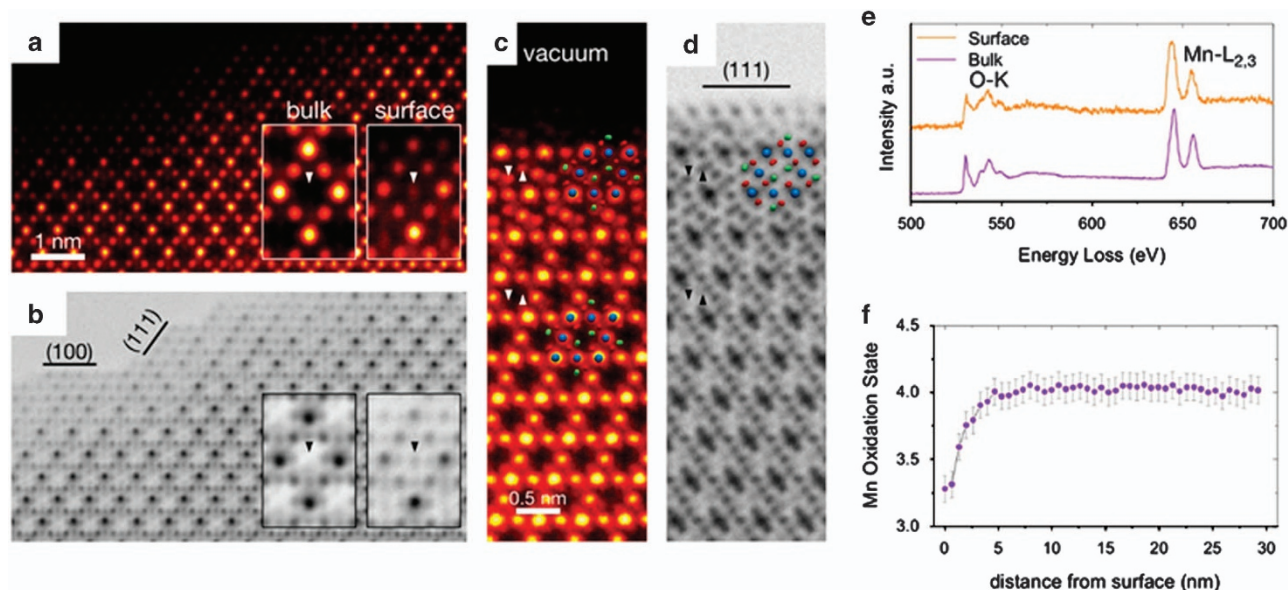


Figure 2 Characterization of the surface atomic and electronic structures of $\text{LiNi}_{0.5}\text{Mn}_{1.5}\text{O}_{4-x}\text{F}_x$ (LNMOF) by scanning transmission electron microscopy (STEM). (a and b) annular dark-field (ADF)- and annular bright-field-STEM (ABF-STEM) images obtained for LNMOF, (c and d) ADF- and ABF-STEM images obtained from the (1 1 1) surface, (e) electron energy-loss spectroscopy (EELS) profiles (O-K and Mn-L_{2,3}) obtained from the top surface and a few nanometers inside this region. (f) Mn oxidation state as a function of distance from the surface using the EELS Mn-L_{2,3} edges.

(Li: 8, Ni: 4, Mn: 12, O: 31, F: 1), $\text{F}_{0.25}$ (Li: 8, Ni: 4, Mn: 12, O: 30, F: 2), and $\text{F}_{0.375}$ (Li: 8, Ni: 4, Mn: 12, O: 29, F: 3)) for our computation. The chemical formula can be described as $\text{LiNi}_{0.5}\text{Mn}_{1.5}\text{O}_{3.875}\text{F}_{0.125}$, where one fluorine anion is substituted with O in the unit cell. We believe that such a negligible difference will not exert any significant effects on these findings.

Figure 1e represents the lattice parameters determined from the XRD patterns and DFT calculations. There was little difference for the $\text{LNMO}_{4-\delta}$ crystals with no F^- substitution, which shows the theoretical validity of our model. The XRD experiments indicated lattice parameter changes that occurred with increasing F^- substitution. The relatively small increase of the lattice parameter in highly fluorinated LNMOF may be from passivation of the oxygen deficiency by the F^- at the defect site. Our calculations predicted a crystal structure transition from a cubic to orthorhombic system with F^- substitution, accompanied by an anisotropic lattice dilatation along the *b*-axis (caused by Jahn–Teller distortion).

We examined the XPS F1s spectral depth profile to elucidate the incompatibility between the experimental and computation results for the lattice parameters (Figures 1f–h). The changes of the F1s core-level spectra as a function of Ar sputtering time represent the intensity of the XPS F1s core-level spectrum, which became extremely weak after the 20 nm etching, and no XPS F1s signals were detected after 40 nm of etching. The remarkable changes in the depth profile indicated that F^- ions were disproportionately incorporated at the crystal surface (which is strongly supported by the DFT calculation). Supplementary Figure S1 represents the energetically most stable atomic arrangements for the surface level at the (a) (1 0 0), (b) (1 1 0) and (c) (1 1 1) plane and for the core level at the (d) (1 0 0), (e) (1 1 0) and (f) (1 1 1) plane in $\text{LiNi}_{0.5}\text{Mn}_{1.5}\text{O}_{4-x}\text{F}_x$ ($x=0.27$ for (1 0 0), $x=0.25$ for (1 1 0) and (1 1 1)). Supplementary Table S2 shows the calculated surface energies from these models; the surface energy of the bulk model was higher than that of the surface model, independent of the crystal faces. F^- preferentially passivated the oxygen vacancy formed at the surface to stabilize the crystal surface. Moreover, the antisite energy for Ni/Mn

ordering decreased with respect to F^- substitution (Supplementary Table S3). The highest F^- substitution ($x=0.375$) made the antisite energy negative, indicating that Ni/Mn disordering preferentially occurred and promoted the phase transition from an ordered to disordered structure.

Mixed F^- influenced the morphology of the LNMOF crystals. The field emission scanning electron microscopy observation clearly visualized the formation of a step-terrace structure at the flat {1 1 1} plane and truncation at the vertices and edges of the parental octahedral structure (Supplementary Figure S1). The truncated lattice faces were assigned to the {1 0 0} faces, bearing a higher surface energy than the {1 1 1} face. Thus, the incorporated F^- potentially reduced the surface energy of the {1 0 0} faces compared with the standard LNMO phase. This is most evident in the atomic-resolution ADF and ABF-STEM images observed in the [1 1 0] crystallographic orientation of LNMOF_{0.2} (Figures 2a and b). The surface is not flat but has two components of the {1 0 0} and {1 1 1} surface steps, which is consistent with the field emission scanning electron microscopy observations in Supplementary Figure S2. A close inspection of the topmost surface indicates that a rock-salt like (similar to nickel oxide) atomic structure was formed at a thickness of a few unit cells, as evident from the cell-averaged inset images in Figures 2a and b: a new atomic site appears on the diamond center, as marked by arrowheads. However, in the {1 1 1} topmost surface, there appears antisite defect spinel structures that seem to form at a thickness of a few unit cells; transition metals might be occupied at Li atomic sites, as marked by arrowheads in Figures 2c and d. Based on the formation of the rock-salt and antisite spinel structure, we conclude that the amount of Li ions is lacking within a few unit cells from the surface because of their elution into water during flux removal.

Figure 2e shows EELS spectra of O-K and Mn-L_{2,3} edges obtained from the topmost surface and bulk regions (10 nm inside of the surface), respectively. Clearly, the intensity of the O-K pre-edge was substantially reduced at the top surface. The Mn oxidation state as a function of distance from the surface, where we

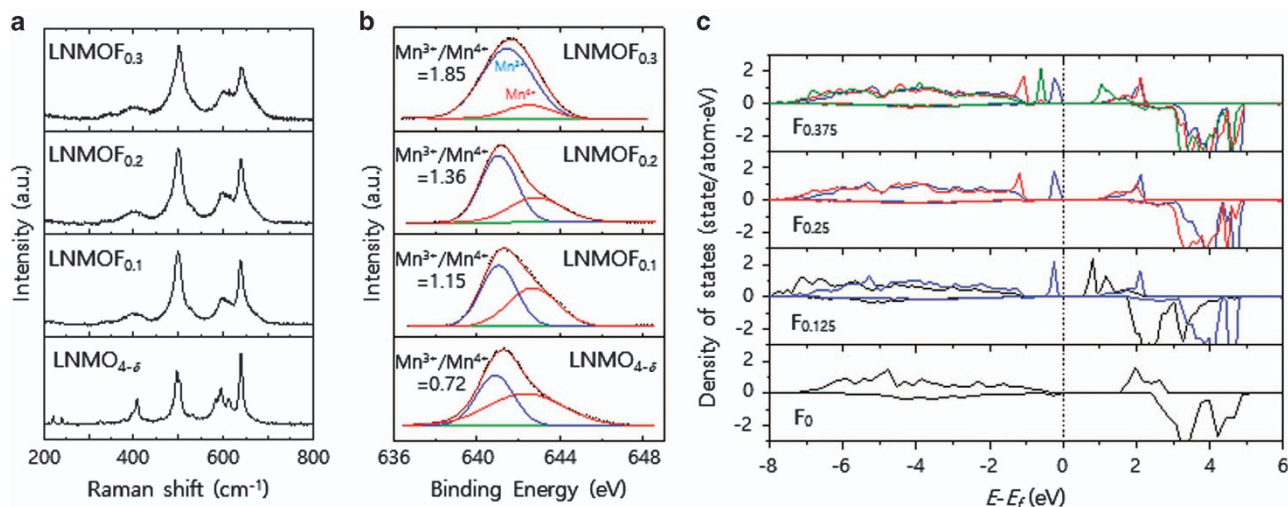


Figure 3 Impact of fluorine anion incorporation on the Ni/Mn arrangements. (a) Raman spectra and (b) X-ray photoelectron spectroscopy (XPS) Mn 2p spectra of LNMOF crystals. The broad peak can be deconvoluted into two peaks, which were assigned to Mn^{3+} (blue) and Mn^{4+} (red) species. (c) Partial densities of state (PDOSs) for the Mn-3d band in $\text{LiNi}_{0.5}\text{Mn}_{1.5}\text{O}_{4-x}\text{F}_x$ ($0 \leq x \leq 0.375$) (black: Mn@OF ; blue: Mn@1F ; red: Mn@2F diagonal; and dark green: Mn@2F neighbor).

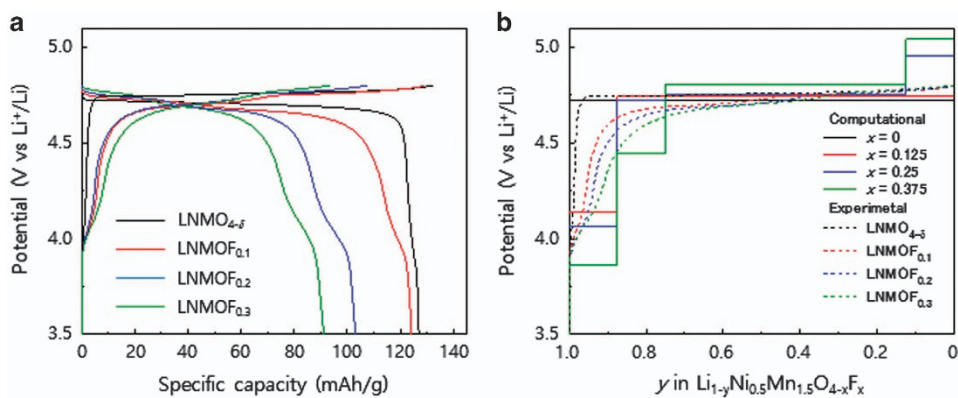


Figure 4 Galvanostatic charge–discharge profiles of $\text{LiNi}_{0.5}\text{Mn}_{1.5}\text{O}_{4-x}\text{F}_x$ (LNMOF) crystal cathodes/Li cells. (a) Galvanostatic charge–discharge curves in the cutoff voltage range of 3.5–4.8 V (0.2 C-rate and 23 °C) and (b) computationally predicted and experimentally obtained voltage profiles during the charging reaction as a function of Li content in the LNMOF systems.

used EELS Mn-L_{2,3} edges, revealed that the Mn oxidation is close to Mn^{3+} and gradually decreased the amount of Mn^{3+} within the top few nanometers of the surface (Figure 2f). Based on both the O-K prepeak reduction and the increase of the Mn^{3+} contents at the surface, we conclude that a certain amount of oxygen vacancies should remain within the top few nanometers of the surface region, despite the incorporation of F^- .

The effect of F^- on the ordering of the Ni/Mn arrangement in the $\text{LNMO}_{4-\delta}$ lattice was studied using Raman spectroscopy. Intense Raman signals at 498 and 638 cm^{-1} (assigned to ordered Ni-O and Mn-O stretching bands, respectively) in the spinel lattice were diminished by the incorporation of F^- independent of the substitution (Figure 3a). The mixed F^- may have highly randomized the Ni/Mn arrangement. The proportion of $\text{Mn}^{3+}/\text{Mn}^{4+}$ examined by XPS (Figure 3b) also strongly supports our consideration. Two peaks attributed to Mn^{3+} and Mn^{4+} were observed in the Mn 2p core-level spectra. The $\text{Mn}^{3+}/\text{Mn}^{4+}$ ratio was 0.72 for the $\text{LNMO}_{4-\delta}$ crystals and increased with F^- substitution, which agrees with our computational predictions (1.15 for $\text{LNMOF}_{0.1}$, 1.36 for $\text{LNMOF}_{0.2}$ and 1.85 for $\text{LNMOF}_{0.3}$). Our DFT calculation also predicted that Mn^{4+} was

reduced to Mn^{3+} in the $\text{LNMO}_{4-\delta}$ lattice when the same number of F^- was introduced.

Figure 3c shows the calculated partial densities of state (PDOSs) for the manganese ions in $\text{LiNi}_{0.5}\text{Mn}_{1.5}\text{O}_{4-x}\text{F}_x$ ($0 \leq x \leq 0.375$). At $x = 0.125$, one Mn-3d band appeared near the Fermi level, indicating that the electron was doped in Mn-3d through the formation of a Mn@1F bond, giving Mn^{3+} . Mn@2F and Mn@1F formed at $x = 0.25$. The Mn-3d bands appeared near the Fermi level. The Mn-3d bands originating from Mn@2F shifted from -0.2 to -1.2 eV, compared with that at $x = 0.125$. Thus, the Mn^{3+} ions were stabilized and became inactive redox couples against the applied voltage of 4.0 V (vs Li^+/Li). This stabilization effect is likely associated with the enhanced Jahn–Teller distortion of Mn^{3+} by the two linearly arranged F^- ions coordinated with Mn^{3+} along the direction parallel to the distortion. At $x = 0.375$, additional Mn-3d bands for Mn@2F appeared at -0.6 eV. Moreover, the antisite energy for Ni/Mn ordering decreased with respect to F^- substitution (Supplementary Table S3). Finally, the highest F^- substitution ($x = 0.375$) made the antisite energy negative, indicating that Ni/Mn disordering preferentially occurred and promoted the phase transition from an ordered to disordered structure.

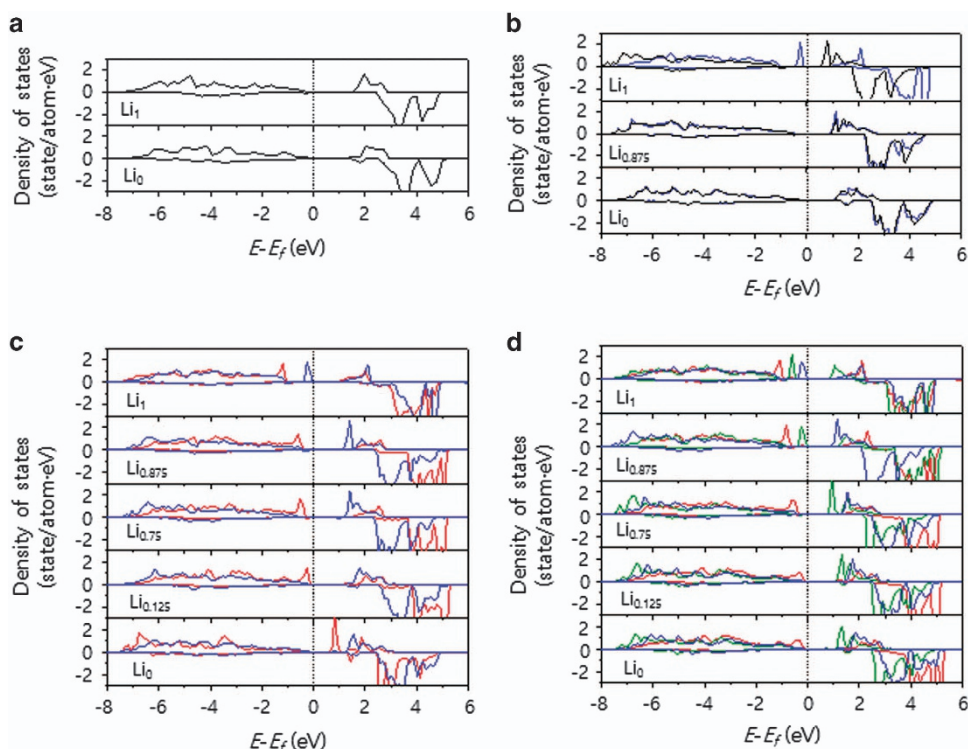


Figure 5 Changes in the partial densities of state (PDOSs) for Mn-3d bands at different lithium compositions. (a) $\text{LiNi}_{0.5}\text{Mn}_{1.5}\text{O}_4$, (b) $\text{LiNi}_{0.5}\text{Mn}_{1.5}\text{O}_{3.875}\text{F}_{0.125}$ (LNMO_{0.1}) (c) $\text{LiNi}_{0.5}\text{Mn}_{1.5}\text{O}_{3.75}\text{F}_{0.25}$ (LNMO_{0.2}) and (d) $\text{LiNi}_{0.5}\text{Mn}_{1.5}\text{O}_{3.625}\text{F}_{0.375}$ (LNMO_{0.3}) (black: Mn@OF; blue: Mn@1F; red: Mn@2F diagonal; and dark green: Mn@2F neighbor).

Galvanostatic charge–discharge tests at various C-rates were systematically performed to examine the effect of F^- substitution on the battery performance, including the rate capability. Figure 4a shows the third charge–discharge cycle profiles at 30 mA g^{-1} , corresponding to a 0.2 C-rate showed that the F^- substitution affected the voltage slope characteristics. Discontinuous sharp changes of the flat voltage were observed in the LNMOF crystals during the charge–discharge reactions from 4.6 to 4.9 V in the discharge reaction, indicating that two redox couples ($\text{Ni}^{2+}/\text{Ni}^{3+}$ and $\text{Ni}^{3+}/\text{Ni}^{4+}$) separately appeared. An inflexion point in the voltage slope at $\sim 4.0 \text{ V}$ was detected, which was assigned to the redox response from $\text{Mn}^{3+}/\text{Mn}^{4+}$. Supplementary Figure S3 shows the cyclic voltammetry of the $\text{LNMO}_{4-\delta}$ and LNMOF crystals. From 4.6 to 4.9 V, two peaks were separated, corresponding to the $\text{Ni}^{2+}/\text{Ni}^{3+}$ and $\text{Ni}^{3+}/\text{Ni}^{4+}$ redox pairs, which were the origin of the voltage step at the lower Li-content region in the voltage profiles (Figure 4a).^{31,48} The $\text{Mn}^{3+}/\text{Mn}^{4+}$ redox peak increased as the mixed F^- increased (caused by charge valence). Meanwhile, the fluorine anion narrowed the potential gap compared with that of $\text{LNMO}_{4-\delta}$ (shown in the redox potential gap for $\text{Ni}^{2+}/\text{Ni}^{3+}$). The reduction of the redox potential gap implies a faster lithiation–delithiation reaction in the disordered Ni/Mn configuration by incorporating F^- .⁴⁹

As shown in Figure 4a, the capacities faded with respect to F^- substitution. The LNMOF_{0.3} cathode/Li cell had the lowest discharge capacity, which was three-quarters of the discharge capacity in the $\text{LNMO}_{4-\delta}$ cathode/Li cell. The DFT calculations provided a full picture of this intriguing phenomenon. The changes in the most stable atomic structure as a function of the Li composition were computed using the formation energies of LNMOF with different atomic arrangements (Supplementary Figure S4). The plausible reaction routes during the charge–discharge reaction and the voltage slopes were computationally predicted (Figure 4b). Our computational

studies duplicated the voltage profile characteristics of the charging process from 3.5 to 5.0 V. The LNMO electrode showed a flat voltage as delithiation at $\sim 4.7 \text{ V}$, assigned to oxidation of Ni^{2+} to Ni^{4+} , whereas the LNMOF electrodes displayed two distinct plateaus at $\sim 4.7 \text{ V}$ and an additional small plateau at $\sim 4.0 \text{ V}$ attributed to the oxidation of Mn^{3+} to Mn^{4+} . There was no intermediate phase once the oxidation state of all manganese ions reached the tetravalent state. Thus, the two-phase region coexisted during the oxidation of Ni^{2+} to Ni^{4+} in the charge process.^{31,50,51} The computational and experimental results indicated that the delithiation energy of LNMO was almost constant for $0 \leq \text{Li} \leq 1$. In contrast, the formation of an oxygen deficiency in the LNMO lattice changed the manganese oxidation state from Mn^{4+} to Mn^{3+} ; a small portion of the manganese remained as Mn^{3+} in the LNMO/Li cell. In fact, crystal growth in a molten salt tends to occur with the lack of oxygen partial pressure, leading to an oxygen defect spinel compared with the solid-state reaction in an oxygen atmosphere.

Our calculations provide new information about the mixed- F^- effects on the electrochemical reaction, including capacity fading. Several voltage steps were observed in both the higher and lower Li-content regions, including a phase transformation triggered by the $\text{Mn}^{3+}/\text{Mn}^{4+}$, $\text{Ni}^{2+}/\text{Ni}^{3+}$ and $\text{Ni}^{3+}/\text{Ni}^{4+}$ oxidation reactions. Higher delithiation energies than that of fully-lithiated LNMO ($\text{Li}=1$) are required in the lower Li-content region ($\text{Li} \leq 0.125$) because of the increased Li vacancy formation energy. The Li ions stored in the LNMOF lattice were not completely electrochemically extracted, causing capacity fade.

The computationally predicted PDOS of LNMOF with different Li compositions showed that the Mn^{3+} ions were oxidized preferentially to Mn^{4+} during the delithiation reaction. For instance, manganese ions show little changes in PDOS when the Li composition is reduced, and,

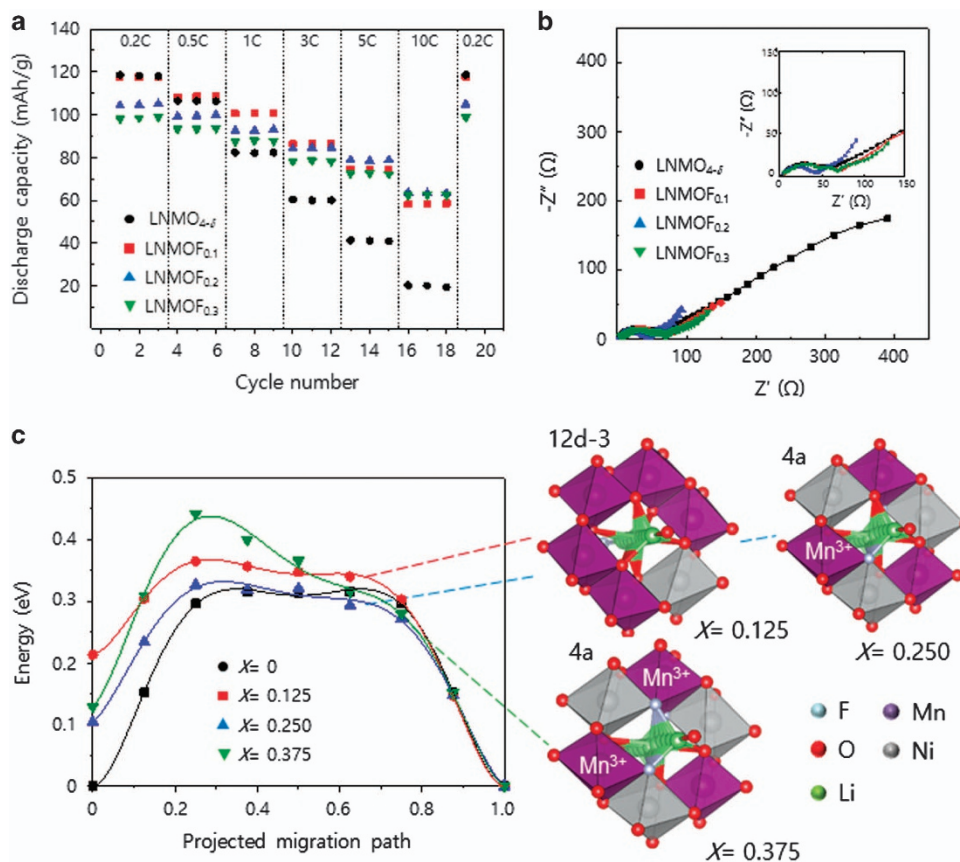


Figure 6 Lithium ion transportational characteristics in the $\text{LiNi}_{0.5}\text{Mn}_{1.5}\text{O}_{4-x}\text{F}_x$ (LNMOF) electrodes. (a) C-rate capabilities and (b) Nyquist plot. The kinetic parameters were determined by electrochemical impedance spectroscopy (EIS) approaches. The Nyquist plots were fitted using the equivalent circuit model. The high- and low-frequency semicircles are attributed to surface film resistance (R_{sf}) and charge transfer resistance (R_{ct}) at the electrode–electrolyte interface, respectively. The Li-ion diffusion coefficient from the relation between the real impedance and the angular frequency in the low-frequency region were further estimated to evaluate quantitatively the F[−]-substitution effects. (c) Lithium ion hopping energy as a function of F content. The calculated energy profiles for lithium-ion hopping along the 8c-4a/12d-8c route with the smallest activation barrier for ion hopping in LNMO and series of LNMOF crystals (12d-3 model in $x=0.125$, 4a model in $x=0.25$ and 4a model in $x=0.375$ in Supplementary Figure 6).

hence, their contribution to the oxidation reaction during delithiation is very small. Figure 5 shows the change in the PDOS for the Mn-3d bands at different Li compositions. The manganese ions formed the Mn@2F arrangement (red line in Figures 5c and d) and did not change their original PDOS profile, even in the delithiated phase, which indicates that they remain in the Mn³⁺ oxidation state. Thus, Mn³⁺ coordinated with two fluorine anions in Mn@2F provided a small contribution to the redox reaction in $\text{Li}_{0.125}\text{Ni}_{0.5}\text{Mn}_{1.5}\text{O}_{4-x}\text{F}_x$ ($0.25 < x \leq 0.375$) through an electrochemical delithiation reaction within the cutoff voltage range of 3.5–4.9 V.

Mn³⁺ bonded with the fluorine anions and required higher potential energies for oxidation: 3.86 V for Mn@1F, 4.44 V for the Mn@2F neighbor and >5.04 V for Mn@2F diagonal in $x=0.375$, compared with that of F[−]-free Mn³⁺. The incorporated F[−] stabilized Mn³⁺ and inhibited its oxidation reaction via the electrochemical delithiation reaction. Two F[−] ions were orthogonally coordinated with Mn³⁺ along the d_{z^2} and $d_{x^2-y^2}$ directions in the Mn@2F neighbor; therefore, one F[−] ion in the Mn@2F orthogonal arrangement stabilized the d_{z^2} orbital and the other F[−] ion stabilized the $d_{x^2-y^2}$ orbital. In contrast, two F[−] ions cooperatively and powerfully stabilized the d_{z^2} orbital of diagonal Mn@2F. These are the most important results for a full understanding of mixed-F[−] effects on the intercalation–deintercalation characteristics of Li manganese oxides with spinel frameworks.

The computationally predicted delithiation characteristics with respect to the coordination numbers of Mn-F bonding were further established using *ex situ* XAFS on the Mn K edge. Changes in the valence states of Mn⁴⁺ in LNMO, LNMOF_{0.1} and LNMOF_{0.3} with different SOC (0 and 75%) were estimated based on the energy shift at 0.9 for the main absorption height. The peak positions and their shifts are summarized in Supplementary Figure S5. A sufficient tendency to explain the effects of fluorine substitution on the capacity fade was observed even though the peak positions with different amounts of F[−] substitution and the peak shift at different SOC were very small. The positions of the absorption peaks at SOC=0% shifted to the lower energy side with increasing F[−]. The formation of the Mn-F coordination bond reduced Mn⁴⁺ to Mn³⁺. Furthermore, all peaks shifted to a higher energy site after charging; thus, Mn³⁺ was oxidized to Mn⁴⁺. Increasing the F[−] substitution decreased the amount of shift. These features strongly support our computational predictions and considerations for the capacity fade of LNMOF.

The C-rate capability was performed to examine the mixed-fluorine-anion effect on the kinetics of Li ion transport. The LNMO_{4- δ} cathode showed the highest discharge capacity at a low current density. However, it showed a greater capacity fade with an increasing current density than that for LNMOF (Figure 6a). While the series of LNMOF cathodes showed a lower discharge capacity at a low C-rate, their capacity dropped because the increased internal

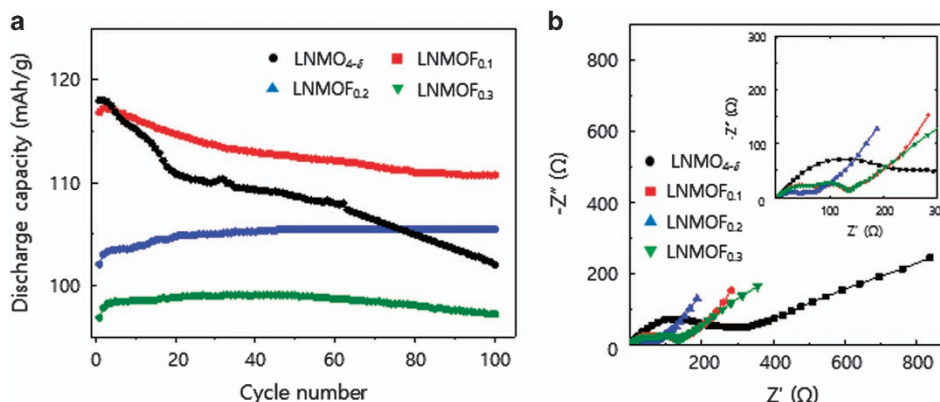


Figure 7 Cycle performances of the $\text{LiNi}_{0.5}\text{Mn}_{1.5}\text{O}_{4-x}\text{F}_x$ (LNMOF) electrodes. (a) Cyclabilities at a 0.2 C-rate, and the discharge capacity vs cycle number for $\text{LNMO}_{4-\delta}$ and a series of LNMOF cathodes/Li cells cycled at 23 °C with a current corresponding to 0.2 °C. (b) Impedance spectra taken after the 100th cycling test at a 0.2 C-rate and 23 °C.

resistance with increasing current density markedly improved. The incorporation of F^- affects the electrochemical Li intercalation kinetics, which are strongly associated with the bulk properties of the electrode materials (e.g., electron conductivity and Li ion conductivity), and the kinetic parameters at the electrode–electrolyte interface.

The kinetic parameters were determined by EIS approaches. Figure 6b shows the Nyquist plots of the $\text{LNMO}_{4-\delta}$ and LNMOF electrodes. The impedance spectra were fitted using the equivalent circuit model. The high- and low-frequency semicircles are attributed to surface film resistance (R_{sf}) and charge transfer resistance (R_{ct}), respectively, at the electrode–electrolyte interface. We further calculated the Li-ion diffusion coefficient from the relation between the real impedance and the angular frequency in the low-frequency region to evaluate quantitatively the F^- -substitution effects. The kinetic parameters are summarized in Supplementary Table S4. Increasing the mixed- F^- content effectively reduced R_{sf} and R_{ct} , and they reached minimum values for $\text{LNMOF}_{0.3}$. Further F^- substitution increased the resistance, which might correspond to disturbed Li ion migration by excess amounts of F^- .

The relationship between Li ion migration and fluorine anion substitution was considered using DFT calculations to predict Li-ion migration paths (Figure 6c). The Li ion in the spinel framework preferentially migrated along the $8c$ - $4a/12d$ - $8c$ route, independent of F^- substitution. In the considerable migration models shown in Supplementary Figure S6, the activation barrier for ion hopping in the LNMO and series of LNMOF crystals was the smallest in the $12d$ -3 model at $x=0.125$ (0.37 eV), $4a$ model at $x=0.25$ (0.33 eV) and $4a$ model at $x=0.375$ (0.44 eV). In particular, the $\text{LNMOF}_{0.2}$ cathode showed minimum activation energies and the highest Li ion conductivity, which agree with the C-rate capability test.

The migration paths and their corresponding activation energy profiles for Li^+ hopping along $8c$ - $4a/12d$ - $8c$ in stoichiometric LNMO, non-stoichiometric $\text{LNMO}_{4-\delta}$ and $\text{LNMOF}_{0.1}$ are summarized in Supplementary Figure S7. These results indicate that the migration path and the activation energy for Li^+ hopping strongly depend on the interaction between V_{Li}' at the $8c$ - $4a/12d$ - $8c$ site and $\text{O}_{\text{O}}^{\times}$, V_{O}^{\times} or F_{O} at the $24e$ site. The Li^+ ion in stoichiometric LNMO moves in a straight line along the migration path, as shown for spinel $\text{Li}_4\text{Ti}_5\text{O}_{12}$.⁴⁶ In contrast, Li^+ in $\text{LNMO}_{4-\delta}$ and $\text{LNMOF}_{0.1}$ migrates tortuously at V_{O}^{\times} and F_{O} , respectively. Replacing V_{O}^{\times} with F_{O} mitigated the tortuous Li^+ migration path and lowered the activation energy from 1 eV to ~ 0.5 eV, as required for Li^+ hopping because the coordination

number of the Li^+ ion at $8c$ - $4a/12d$ - $8c$ in $\text{LNMOF}_{0.1}$ remained three (two oxygen and one fluorine), even though that of LNMO was two (two oxygen).

Li-ion hopping can be interpreted as Li ion vacancy (V_{Li}') hopping. Generally, the valence state for V_{Li}' is negatively charged. Therefore, F_{O} slightly changed the charged state of the $4a/12d$ site (V_{Li}') and became more positive because of the different valence states. The activation barrier for Li-ion hopping along the $8c$ - $4a/12d$ - $8c$ path became larger because the Li ion path was more positively charged. In other words, V_{Li}' is strongly trapped with F_{O} because of defect aggregation. In contrast, the DFT calculations revealed that incorporating F^- strongly affected Li ion conductivity in non-stoichiometric $\text{LNMO}_{4-\delta}$ with V_{O}^{\times} . The charged state of the $4a/12d$ site in non-stoichiometric LNMO became much more positive after the formation of a V_{O}^{\times} at the $24e$ site compared with that of stoichiometric LNMO. Replacing V_{O}^{\times} at the $24e$ site with F_{O} reduced the activation energy for Li-ion hopping because of the relaxed electrostatic repulsion at the $4a/12d$ site of $\text{LNMO}_{4-\delta}$, which was positively charged.

Fluorine anion substitution-dependent changes to the Li-ion hopping route were not seen; however, their activation barrier changed significantly with respect to the symmetry in the site potential of the two tetrahedral $8c$ sites adjacent to the octahedral $4a/12d$ sites in the Li-ion diffusion path. A symmetric site potential across $8c$ - $4a$ - $8c$ was formed in $\text{LNMOF}_{0.2}$ by the substitution of a single F^- in both tetrahedral $8c$ sites, leading to a site potential minimum (which is in contrast to those of asymmetric $\text{LNMOF}_{0.1}$ and $\text{LNMOF}_{0.3}$, whose activation barriers were higher than that of $\text{LNMOF}_{0.2}$). Oxygen vacancies in the two tetrahedral $8c$ sites adjusted to the octahedral $4a/12d$ site and were inhomogeneously substituted with F^- to form different Li-F coordination numbers in $\text{LNMOF}_{0.1}$ ($\text{Li}_{8c}^x@1\text{F}_{24e}\text{-Li}_{8c}^x@24e^x$) and $\text{LNMOF}_{0.3}$ ($\text{Li}_{8c}^x@1\text{F}_{24e}\text{-Li}_{8c}^x@2\text{F}_{24e}$), which imbalanced the site potential and increased the activation barrier for ion hopping. These calculations agreed with the experimentally demonstrated C-rate capability and EIS results.

Figure 7a shows the discharge capacity vs cycle number for $\text{LNMO}_{4-\delta}$ and a series of LNMOF cathodes/Li cells cycled at 23 °C with a current corresponding to 0.2 °C. A significant capacity loss with cycle number was observed to 80% of the initial capacity for the $\text{LNMO}_{4-\delta}$ /Li cells after 100 cycles; all of the fluorine-substituted LNMOF/Li cells showed an obvious improvement in the cyclability with capacity retentions $> 90\%$. The $\text{LNMOF}_{0.2}$ /Li cell showed almost no capacity loss during cycling. The coulomb efficiency of the cell was

almost constant at ~ 0.990 during the cycles. Furthermore, EIS experiments for the cells after 100 cycles (Figure 7b) showed that the all-kinetic parameters (R_{sf} , R_{ct} and D_{Li}) degraded with cycling; however, the deterioration of the LNMOF_{0.2}/Li cell was significantly smaller (Supplementary Table S5). Fluorine anion substitution likely suppressed the dissolution of the manganese ion into the electrolyte and metal-fluoride formation as a solid electrolyte interface by oxidative decomposition of the liquid electrolyte at high voltages. The computational studies implied that the stabilization of Mn³⁺ by neighboring F⁻ (formation of coordination bonds and enhancement of Jahn–Teller distortion) primarily contributed to the significant cyclability improvement. Furthermore, we reported that surface modifications of the LNMO crystals with <2-nm-thick fluoroalkylsilane monolayers improved the cyclability by enhancing the lyophobic characteristics against liquid electrolytes.³⁵ The mixed F⁻ lowered the surface energy by inducing segregation near the surface. A similar surface modification was imparted by the fluoroalkylsilane monolayer and will contribute in improving the cycle characteristics. Based on the changes in the Mn³⁺/Mn⁴⁺ ratio of the XPS-Mn core-level spectra taken from the electrode surface after cycling, we showed that Mn³⁺ does not go through the notorious disproportionation reaction. The absence ratio of Mn³⁺ was sufficiently retained in the LNMO stabilized with the fluoroalkylsilane monolayer compared with that of bare LNMO. Furthermore, retention of dark pigments was observed on the polypropylene separator after 100 cycles in the LNMO/Li cell, unlike that in the LNMOF_{0.2}/Li cells. The batteries were reusable after replacing an old separator with a new one. These results strongly suggest that the incorporation of F⁻ into the LNMO lattice prevents the risk for higher capacity fading under high-voltage operation because of the occurrence of a short circuit caused by Mn³⁺ dissolution during cycling.

In summary, we determined the effect of mixed-fluorine anions in oxygen-deficient, spinel-type LNMO_{4- δ} crystals on the structural, electrical and electrochemical characteristics by experimental and computational approaches. This is the first report that provides the full picture for mixed-fluorine-anion effects on high-voltage spinel manganese cathodes. The anion-mixed effects are an exciting new direction for the development of high-voltage cathode materials.

CONFLICT OF INTEREST

The authors declare no conflict of interest.

ACKNOWLEDGEMENTS

This work was partially supported by JST-CREST (JPMJCR1322), Japan. GSS, RI and YI acknowledge the Research Hub for Advanced Nano Characterization, the University of Tokyo, under the support of 'Nanotechnology Platform' (project no. 12024046) by MEXT, Japan.

- 1 Armand, M. & Tarascon, J. M. Building better batteries. *Nature* **451**, 652–657 (2008).
- 2 Winter, M. & Brodd, R. J. What are batteries, fuel cells, and supercapacitors? *Chem. Rev.* **104**, 4245–4270 (2004).
- 3 Padhi, A. K., Nanjundaswamy, K. S. & Goodenough, J. B. Phospho-olivines as positive-electrode materials for rechargeable lithium batteries. *J. Electrochem. Soc.* **148**, 1188–1194 (1997).
- 4 Liu, G. Q., Wen, L. & Liu, Y. M. LiNi_{0.5}Mn_{1.5}O₄ and its derivatives as cathodes for high-voltage Li-ion batteries. *J. Solid State Electrochem* **14**, 2191–2202 (2010).
- 5 Santhanam, R. & Rambabu, B. Research progress in high voltage spinel LiNi_{0.5}Mn_{1.5}O₄ material. *J. Power Sources* **195**, 5442–5451 (2010).
- 6 Goodenough, J. B. & Kim, Y. Challenges for rechargeable Li batteries. *Chem. Mater.* **22**, 587–603 (2010).

- 7 Shiiba, H., Zettsu, N., Nakayama, M., Oishi, S. & Teshima, K. Defect formation energy in spinel LiNi_{0.5}Mn_{1.5}O_{4- δ} using *ab initio* DFT calculations. *J. Phys. Chem. C* **119**, 9117–9124 (2015).
- 8 Terada, Y., Yasaka, K., Nishikawa, F., Konishi, T., Yoshio, M. & Nakai, I. *In situ* XAFS analysis of Li(Mn, M)₂O₄ (M=Cr, Co, Ni) 5V cathode materials for lithium-ion secondary batteries. *J. Solid State Chem.* **156**, 286–291 (2001).
- 9 Dokko, K., Mohamedi, M., Anzue, N., Itoh, T. & Uchida, I. *In situ* Raman spectroscopic studies of LiNi_{0.5}Mn_{1.5}O₄ thin film cathode materials for lithium ion secondary batteries. *J. Mater. Chem.* **12**, 3688–3693 (2002).
- 10 Yang, T., Zhang, N., Lang, Y. & Sun, K. Enhanced rate performance of carbon-coated LiNi_{0.5}Mn_{1.5}O₄ cathode material for lithium ion batteries. *Electrochim. Acta* **56**, 4058–4064 (2011).
- 11 Wang, L., Li, H., Huang, X. & Baudrin, E. A comparative study of Fd-3m and P4₃32 "LiNi_{0.5}Mn_{1.5}O₄". *Solid State Ionics* **193**, 32–38 (2011).
- 12 Kunduraci, M., Al-Sharab, J. F. & Amatucci, G. G. High-power nanostructured LiMn_{2- x} Ni _{x} O₄ high-voltage lithium-ion battery electrode materials: electrochemical impact of electronic conductivity and morphology. *Chem. Mater.* **18**, 3585–3592 (2006).
- 13 Verhoeven, V. W. J., Mulder, F. M. & de Schepper, I. M. Influence of Mn by Li substitution on the Jahn–Teller distortion in LiMn₂O₄. *PhysB* **276**, 950–951 (2000).
- 14 Singh, G., Gupta, S. L., Prasad, R., Auluck, S., Gupta, R. & Sil, A. Suppression of Jahn–Teller distortion by chromium and magnesium doping in spinel LiMn₂O₄ a first-principles study using GGA and GGA+U. *J. Phys. Chem. Solids* **70**, 1200–1206 (2009).
- 15 Ouyang, C. Y., Shi, S. Q. & Lei, M. S. Jahn–Teller distortion and electronic structure of LiMn₂O₄. *J. Alloys Compd.* **474**, 370–374 (2009).
- 16 Park, S. H. & Sun, Y. K. Synthesis and electrochemical properties of 5 V spinel LiNi_{0.5}Mn_{1.5}O₄ cathode materials prepared by ultrasonic spray pyrolysis method. *Electrochim. Acta* **50**, 434–439 (2004).
- 17 Yi, T. F., Xie, Y., Ye, M. F., Jiang, L. J., Zhu, R. S. & Zhu, Y. R. Recent developments in the vDoping of LiNi_{0.5}Mn_{1.5}O₄ cathode material for 5 V lithium-ion batteries. *Ionics* **17**, 383–389 (2001).
- 18 Zhong, G. B., Wang, Y. Y., Zhang, Z. C. & Chen, C. H. Effects of Al substitution for Ni and Mn on the electrochemical properties of LiNi_{0.5}Mn_{1.5}O₄. *Electrochim. Acta* **56**, 6554–6561 (2011).
- 19 Aklalouch, M., Amarilla, J. M., Rojas, R. M., Saadoun, I. & Rojo, J. M. Chromium doping as a new approach to improve the cycling performance at high temperature of 5 V LiNi_{0.5}Mn_{1.5}O₄-based positive electrode. *J. Power Sources* **185**, 501–511 (2008).
- 20 Ito, A., Li, D., Lee, Y., Kobayakawa, K. & Sato, Y. Influence of Co substitution for Ni and Mn on the structural and electrochemical characteristics of LiNi_{0.5}Mn_{1.5}O₄. *J. Power Sources* **185**, 1429–1433 (2008).
- 21 Oh, S. H., Chung, K. Y., Jeon, S. H., Kim, C. S., Cho, W. I. & Cho, B. W. Structural and electrochemical investigations on the LiNi_{0.5- x} Mn_{1.5- x} M _{x} O₄ (M=Cr, Al, Zr) compound for 5V cathode material. *J. Alloys Compd.* **469**, 244–250 (2009).
- 22 Park, S. B., Eom, W. S., Cho, W. I. & Jang, H. Electrochemical properties of LiNi_{0.5}Mn_{1.5}O₄ cathode after Cr doping. *J. Power Sources* **159**, 679–684 (2006).
- 23 Wang, H., Xia, H., Lai, M. O. & Lu, L. Enhancements of rate capability and cyclic performance of spinel LiNi_{0.5}Mn_{1.5}O₄ by trace Ru-doping. *Electrochem. Commun.* **11**, 1539–1542 (2009).
- 24 Alcantara, R., Jaraba, M., Lavela, P., Tirado, J. L., Zhecheva, E. & Stoyanova, R. Changes in the local structure of LiMg _{x} Ni_{0.5- x} Mn_{1.5}O₄ electrode materials during lithium extraction. *Chem. Mater.* **16**, 1573–1579 (2004).
- 25 Liu, J. & Manthiram, A. Understanding the improved electrochemical performances of Fe-substituted 5 V spinel cathode LiNi_{0.5}Mn_{1.5}O₄. *J. Phys. Chem. C* **113**, 15073–15079 (2009).
- 26 Schroeder, M., Glatthaar, S., Geßwein, H., Winkler, V., Bruns, M., Scherer, T., Chakravadhanula, V. S. K. & Binder, J. R. Post-doping via spray-drying: a novel sol-gel process for the batch synthesis of doped LiNi_{0.5}Mn_{1.5}O₄ spinel material. *J. Mater. Sci.* **48**, 3404–3414 (2013).
- 27 Wen, W., Ju, B., Wang, X., Wu, C., Shu, H. & Yang, X. Effects of magnesium and fluorine Co-doping on the structural and electrochemical performance of the spinel LiMn₂O₄ cathode materials. *Electrochim. Acta* **147**, 271–278 (2014).
- 28 Hagh, N. M. & Amatucci, G. G. Effect of cation and anion doping on microstructure and electrochemical properties of the LiNi_{0.5}Mn_{1.5}O_{4- δ} spinel. *J. Power Sources* **256**, 457–469 (2014).
- 29 Oh, S. W., Park, S. H., Kim, J. H., Bae, Y. C. & Sun, Y. K. Improvement of electrochemical properties of LiNi_{0.5}Mn_{1.5}O₄ spinel material by fluorine substitution. *J. Power Sources* **157**, 464–470 (2006).
- 30 Du, G., NuLi, Y., Yang, J. & Wang, J. Fluorine-doped LiNi_{0.5}Mn_{1.5}O₄ for 5v cathode materials of lithium-ion battery. *Mater. Res. Bull.* **43**, 3607–3613 (2008).
- 31 Lee, E. & Persson, K. A. Revealing the coupled cation interactions behind the electrochemical profile of Li _{x} Ni_{0.5}Mn_{1.5}O₄. *Energy Environ. Sci.* **5**, 6047–6051 (2012).
- 32 Schmidt, R., Basu, A. & Brinkman, A. W. Small polaron hopping in spinel manganates. *Phys. Rev. B* **72**, 115101–115110 (2005).
- 33 Schmidt, R., Basu, A., Brinkman, A. W., Klusek, Z. & Datta, P. K. Electron-hopping modes in NiM₂O_{4+ δ} materials. *Appl. Phys. Lett.* **86**, 073501–073504 (2005).
- 34 Xiao, J., Chen, X., Sushko, P. V., Sushko, M. L., Kovarik, L., Feng, J., Deng, Z., Zheng, J., Graff, G. L., Nie, Z., Choi, D., Liu, J., Zhang, J. G. & Whittingham, M. S. High-performance LiNi_{0.5}Mn_{1.5}O₄ spinel controlled by Mn³⁺ concentration and site disorder. *Adv. Mater.* **24**, 2109–2116 (2012).
- 35 Zettsu, N., Kida, S., Uchida, S. & Teshima, K. Sub-2 nm thick fluoroalkylsilane self-assembled monolayer-coated high voltage spinel crystals as promising cathode materials for lithium ion batteries. *Sci. Rep.* **6**, 31999 (2016).

- 36 Kresse, G & Furthmuller, J. Efficient iterative schemes for *ab initio* total-energy calculations using a plane-wave basis set. *Phys. Rev. B* **54**, 11169–11186 (1996).
- 37 Kresse, G & Furthmuller, J. Efficiency of *ab-initio* total energy calculations for metals and semiconductors using a plane-wave basis set. *Comput. Mater. Sci.* **6**, 15–50 (1996).
- 38 Perdew, J. P., Ruzsinszky, A., Csonka, G. I., Vydrov, O. A., Scuseria, G. E., Constantin, L. A., Zhou, X. & Burke, K. Restoring the density-gradient expansion for exchange in solids and surfaces. *Phys. Rev. Lett.* **100**, 136406–136409 (2008).
- 39 Blöchl, P. E. Projector augmented-wave method. *Phys. Rev. B* **50**, 17953–17979 (1994).
- 40 Jain, A, Hautier, G., Ong, S. P., Moore, C. J., Fischer, C. C., Persson, K. A. & Ceder, G. Formation enthalpies by mixing GGA and GGA+U calculations. *Phys. Rev. B* **84**, 045115 (2011).
- 41 Muller, T, Hautier, G, Jain, A & Ceder, G. Evaluation of favorite-structured cathode materials for lithium-ion batteries using high-throughput computing. *Mater. Chem.* **23**, 3854–3862 (2011).
- 42 Hautier, G, Ong, S. P, Jain, A, Moore, C. J & Ceder, G. Accuracy of density functional theory in predicting formation energies of ternary oxides from binary oxides and its implication on phase stability. *Phys. Rev. B* **85**, 155208 (2012).
- 43 Biškup, N., Martínez, J.L., Arroyo de Dompablo, M. E., Díaz-Carrasco, P. & Morales, J. Relation between the magnetic properties and the crystal and electronic structures of manganese spinels $\text{LiNi}_{0.5}\text{Mn}_{1.5}\text{O}_4$ and $\text{LiCu}_{0.5}\text{Mn}_{1.5}\text{O}_{4-\delta}$ ($0 < \delta < 0.125$). *J. Appl. Phys.* **100**, 093908 (2006).
- 44 Amdouni, N., Zaghib, K., Gendron, F., Mauger, A. & Julien, C. M. Magnetic properties of $\text{LiNi}_{0.5}\text{Mn}_{1.5}\text{O}_4$ spinels prepared by wet chemical methods. *J. Magn. Magn. Mater.* **309**, 100–105 (2007).
- 45 Chen, Y., Sun, Y. & Huang, X. Origin of the Ni/Mn ordering in high-voltage spinel $\text{LiNi}_{0.5}\text{Mn}_{1.5}\text{O}_4$: the role of oxygen vacancies and cation doping. *Comp. Mater. Sci.* **115**, 109–116 (2016).
- 46 Shiiba, H., Nakayama, M. & Nogami, M. Ionic conductivity of lithium in spinel-type $\text{Li}_{4/3}\text{Ti}_{5/3}\text{O}_4\text{-LiMg}_{1/2}\text{Ti}_{3/2}\text{O}_4$ solid-solution system. *Solid State Ionics* **181**, 994–1001 (2010).
- 47 Jonsson, H., Mills, G., Jacobsen, K. W., Berne, B. J. in *Classical and Quantum Dynamics in Condensed Phase Simulations* (eds Chandler D., Berne B. J., Ciccotti G. & Coker D. F.) 385–404 (World Scientific: Singapore, 1998).
- 48 Sushko, P. V., Rosso, K. M., Zhang, J. G., Liu, J. & Sushko, M. L. Oxygen vacancies and ordering of D-levels control voltage suppression in oxide cathodes: the case of spinel $\text{LiNi}_{0.5}\text{Mn}_{1.5}\text{O}_{4-\delta}$. *Adv. Funct. Mater.* **23**, 5530–5535 (2013).
- 49 Jafta, C. J., Mathe, M. K., Manyala, N., Roos, W. D. & Ozoemena, K. I. Microwave-assisted synthesis of high-voltage nanostructured $\text{LiNi}_{0.5}\text{Mn}_{1.5}\text{O}_4$ spinel: tuning the Mn^{3+} content and electrochemical performance. *Appl. Mater. Interfaces* **5**, 7592–7598 (2013).
- 50 Xia, H., Meng, Y. S., Lu, L. & Ceder, G. Electrochemical properties of nonstoichiometric $\text{LiNi}_{0.5}\text{Mn}_{1.5}\text{O}_{4-\delta}$ thin-film electrodes prepared by pulsed laser deposition. *J. Electrochem. Soc.* **154**, A737–A743 (2007).
- 51 Kim, J. H., Myung, S. T., Yoon, C. S., Kang, S. G. & Sun, Y. K. Comparative study of $\text{LiNi}_{0.5}\text{Mn}_{1.5}\text{O}_{4-\delta}$ and $\text{LiNi}_{0.5}\text{Mn}_{1.5}\text{O}_4$ cathodes having two crystallographic structures: Fd-3M and P4₃32. *Chem. Mater.* **16**, 906–914 (2004).



This work is licensed under a Creative Commons Attribution 4.0 International License. The images or other third party material in this article are included in the article's Creative Commons license, unless indicated otherwise in the credit line; if the material is not included under the Creative Commons license, users will need to obtain permission from the license holder to reproduce the material. To view a copy of this license, visit <http://creativecommons.org/licenses/by/4.0/>

© The Author(s) 2017

Supplementary Information accompanies the paper on the NPG Asia Materials website (<http://www.nature.com/am>)